

# Fracture characterization in tubular LSFCE ceramic membranes

N. Nagendra<sup>a,\*</sup>, R.F. Klie<sup>b</sup>, N.D. Browning<sup>b</sup>, S. Bandhopadhyay<sup>a</sup>

<sup>a</sup> School of Mineral Engineering, University of Alaska, Fairbanks, AK 99709, USA

<sup>b</sup> Department of Physics, University of Illinois at Chicago, Chicago, IL 60607, USA

Received 30 November 2001; received in revised form 4 April 2002

## Abstract

Lanthanum based perovskite oxides are subject of extensive studies for application as oxygen-separation membranes where they are designed to be used as tubes in advanced reactors. In the present study, tubular  $\text{La}_{0.2}\text{Sr}_{0.8}\text{Fe}_{0.8}\text{Cr}_{0.2}\text{O}_{3-\delta}$  perovskite membrane has been evaluated for structural properties viz. fracture strength in two different conditions: ambient and in  $\text{N}_2$  at 1000 °C and 0.17 MPa. The results show that in the slightly reducing condition, the fracture strength of the perovskite tubes decrease to nearly half its value at ambient conditions (186 and 307 MPa, respectively) with a negligible change in the Weibull modulus ( $m$ ). The fracture origins are primarily processing related surface and volume flaws. Microscopic analysis indicates that fracture is brittle and by transgranular cleavage. In reducing conditions, there is a drastic change in fracture morphology and can be argued as being aided by creation of excess oxygen defects in the membrane. A strong correlation is observed to exist between the fracture strength, fracture morphology and defect chemistry in a tubular LSFCE membrane.

© 2002 Elsevier Science B.V. All rights reserved.

**Keywords:** Perovskite membrane; Fracture strength; Weibull modulus; Brownmillerite; Transgranular fracture

## 1. Introduction

Oxygen ion-conducting ceramic membranes are being investigated for applications such as oxygen separators, catalytic membrane reactors and solid oxide fuel cells (SOFCs), etc. The main factors driving the renewed interest in these materials are increasing emphasis on energy efficiency and reduced environmental emissions. For the applications mentioned above, the ceramic membrane has to be dense and most importantly, must have high oxygen ion conductivity. The high oxygen ion conductivity implies ionic transport by the motion of suitable point defects (generally oxygen vacancies) through the oxide lattice. For this reason, the oxides being developed often have fluorite-related or perovskite-related crystal structures since these are known to be capable, on appropriate doping, of accommodating large concentrations of mobile oxygen ions. Moreover, oxygen vacancies in many of these materials can also be created by exposure to an

environment having a sufficiently low thermodynamic oxygen activity—for example a reducing gas.

In the case of one of the most widely studied and applied class of ceramic membranes, the perovskite oxides ( $\text{ABO}_3$ ), atomic scale defects control extensive material properties, such as color, diffusion, ionic conductance, luminescence, magnetic susceptibility, and superconductivity [1,2].  $\text{ABO}_3$  on doping (for example: Sr on the A site and Cr on the B site in  $\text{LaFeO}_3$  lattice) can assume structural variations and also can accommodate very large concentrations of anion vacancies in their structures [3]. Doped  $\text{ABO}_3$  compositions of the general class  $(\text{La}_x\text{Sr}_{1-x})(\text{Fe}_y\text{Cr}_{1-y})\text{O}_{3-\delta}$  [LSFCE] are in particular targeted for applications as solid oxide fuel cells, ceramic-oxygen separation membranes (SynGas reactors) and electrodes at high temperature. These oxides under steep oxygen pressure gradients are shown to exhibit many useful properties, such as high temperature stability, high mechanical stability, high point defect acceptance and low thermal expansion coefficient at operating temperatures [4]. The above-mentioned physical properties are related to the oxygen stoichiometry, which is wholly dependent on temperature and oxygen

\* Corresponding author

E-mail address: ffn@uaf.edu (N. Nagendra).

partial pressure. The oxygen non-stoichiometry in these oxides has been shown to be controlled by the substitution of lower valence cations on the A site (e.g. of  $\text{Sr}^{2+}$  in place of  $\text{La}^{3+}$ ) [5]. Similar studies have also concluded that: (a) instability of perovskite by A site Sr doping can be compensated by Fe multi-valence states; and (b) B site Ti and Cr doping can enhance the necessary stability of single phase perovskites.

An important issue in the development of perovskite-type oxygen conducting membranes has been the structural, chemical and mechanical stability of the materials at high temperatures and in reducing environments. In recent years, extensive micro-structural evaluations have been performed in an effort to understand the structure-property relationships of several technologically relevant crystalline perovskite oxides [6–11]. The studies have subsequently thrown much light on the structure-property relationships existing at the atomic scale influencing material behavior such as conductivity, etc. [12]. In particular, studies using Z-contrast imaging and electron energy loss spectroscopy (EELS) have shown the ability to correlate precisely the atomic features controlling the materials properties at temperatures close to the standard operating conditions [13].

However, up to date, there are insufficient experimental data to extend such relationships to a macro-level to explain mechanical properties such as strength, toughness, etc. important for structural design. For gas separation, structural design necessitates that the oxides are used as tubes (rather than bars or plates) at high temperature and pressure. The reducing conditions as encountered in a reactor environment can be expected to bear significant influence on the mechanical properties of the oxides membranes. Also, factors such as: gradation in concentration of oxygen vacancies across the thickness; chemically induced stress are strongly dependent on the variation of non-stoichiometry and geometry of the membrane. These factors often can induce or enhance mechanical stresses leading to fracture in the oxide membrane. Additionally, the tubular geometry of the membranes amplifies the complexity of thermal and mechanical stresses encountered in the reactor. For this reason much of the available mechanical property data on perovskite oxides (Gallates, Chromites, etc. from fuel cells literature) obtained from laboratory testing of regular specimens such as bend bars [14–21] are not a very good estimate for reactor design. Evaluation of reliable mechanical properties of the oxides tubes in its operating conditions is thus of critical importance for improved design of a gas separation unit.

In the present paper, LSCFO perovskite tubes have been tested for strength at ambient and in  $\text{N}_2$  at 1000 °C and 0.17 MPa. With the broad objectives mentioned in the preceding paragraphs, C-ring tests were chosen for strength evaluation of oxide tubes. For a C-ring test, the specimen preparation is simple and

since the maximum tensile stress is generated along the outer diameter, results are sensitive to surface flaws or changes in surface flaw distribution induced by environmental factors. The tests indicate that various macroscopic defects such as processing related flaws influence the strength distribution of the oxide membrane. The study is further extended and initial attempts have been made to co-relate macro/microscopic aspects of fracture with atomic scale defects analyzed by scanning transmission electron microscopy.

## 2. Experimental procedure

LSCFO membranes of the general composition  $\text{La}_{0.2}\text{Sr}_{0.8}\text{Fe}_{0.8}\text{Cr}_{0.2}\text{O}_{3-\delta}$  were provided for testing by BP Chemicals, USA. The oxide membranes are processed as tubes by a proprietary process involving cold-isostatic pressing and sintering of the base powder with the above composition. The base powder was prepared using the modified Pechini or polymer precursor synthesis method [22,23]. Rings of dimension as shown in Table 1 were cut from the tubes in a low speed saw. The surfaces of the rings were ground and polished to a 1  $\mu\text{m}$  finish using successive grades of SiC paper and finally with a diamond compound. The edges of the rings were chamfered to ensure that preferential failures from edge flaws were minimized. The rings are subsequently notched by a 0.5 mm low speed saw to form a C-ring specimen [24,25]. The C-rings were placed in an autoclave (to ensure uniform temperature and humidity) between two alumina platens in a hydraulic testing frame (MTS 858 MiniBionix II). Stabilized Zirconia cloth (0.5 mm) as pressure pads were used to reduce frictional stresses and to prevent slippage of the rings during testing (Fig. 1). To ensure that the tests yielded reproducible values, initial tests were done on commercially available and surface finished Alumina (99.8%) tubes. For high temperature studies, the autoclave chamber was flushed with ultra high purity (UHP)  $\text{N}_2$  and a positive chamber pressure of 0.17 MPa maintained. The chamber temperature was then raised at 10 °C  $\text{min}^{-1}$  to the final temperature of 1000 °C. The test conditions are slightly reducing with measured oxygen equilibrium partial pressure corresponding to  $\log_{\text{PO}_2} = (-4)$ . The rings were soaked for a period of 15 min at the testing temperature prior to application of load. All the tests were done by monotonically loading in diametral compression to fracture at a constant crosshead speed of 0.5 mm  $\text{min}^{-1}$ . After testing, the outer surfaces exposed to the environment were analyzed to determine phases separation if any in a Siemens D5000  $\theta/\theta$  diffractometer using Cu radiation at 40 kv/30 ma. The samples were tested in a parallel beam arrangement to minimize the displacement errors caused by the curved surfaces. The fractured surfaces were

Table 1  
Sample dimensions of C-ring specimens

Sample	Outer radius ( $r_o$ ), mm	Inner radius ( $r_i$ ), mm	Average thickness ( $t$ ), mm	No. samples ( $n$ )	Average strength (MPa)	Weibull Parameter $m$
Alumina	4.8	3.18	1.6	12	229	16
LSFCO (RT)	5.75	4.65	1.1	12	307	4
LSFCO (HT)	5.75	4.65	1.1	12	182	4.8

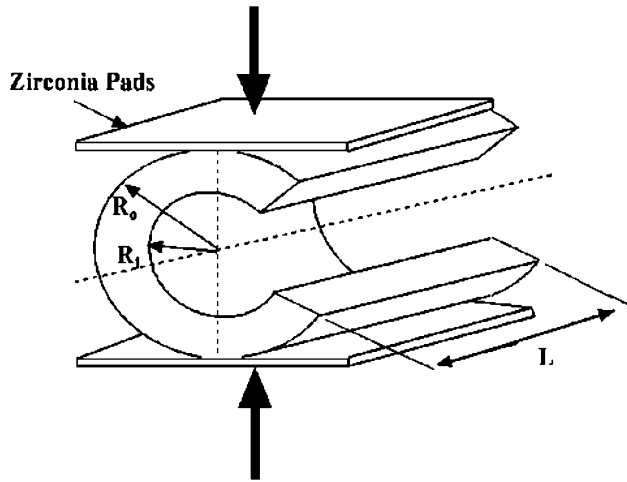


Fig. 1. C-ring specimen configuration for strength analysis.

examined under scanning electron microscope to characterize the dominating flaws and fracture mechanisms.

For analysis of atomic scale structure–property relationships, representative samples of the same composition were exposed to similar reducing conditions. The experimental Z-contrast images [26] and EEL spectra [27] in this study were obtained from a JEOL 2010F field emission STEM/TEM operating at 200 kV [28]. For the in-situ heating experiments, a Gatan double tilt heating holder was used, with a variable temperature range between 293 and 1273 K. The specimen drift obtained with this holder is less than 1 nm per minute for temperatures below 773 K. The oxygen partial pressure in the microscope column is during the experiment  $P_{O_2} \sim 5 \times 10^{-8}$  Pa (i.e. a highly reducing atmosphere). The lens conditions in the microscope were defined for a probe-size of 0.2 nm, with a convergence angle of 13 mrad and a collection angle of 52 mrad. With these settings the Z-contrast image is essentially incoherent [26], i.e. a direct image of the structure, and the resolution of the energy loss spectrum (defined by the FWHM of zero-loss peak) is 1.2 eV at a dispersion of 0.2 eV pixel<sup>-1</sup>. Greater details about sample preparation and microscopic techniques are described elsewhere [28].

### 3. Results and discussions

The test specimens used in this study had an average grain size of 5  $\mu$ m and sub micrometer (0.2–0.5) sized pores were located predominantly at triple points and along grain boundaries. XRD measurements of the sintered material at room temperature indicated that the test specimens had a single-phase perovskite structure. The fracture toughness of the perovskite as measured by indentation method [29] was approximately 1–1.5 MPa m<sup>1/2</sup>.

#### 3.1. Strength distribution

The fracture strength of the C-Ring specimens were calculated from the equation:

$$\sigma_{\theta_{\max}} = \frac{PR}{btr_o} \left[ \frac{r_o - r_a}{r_a - R} \right] \quad (1)$$

where  $r_o$  is the outer radius of the C-Ring;  $b$  is the width;  $t$  is thickness;  $P$  the measured fracture load;  $r_a = (r_o + r_i)/2$  and  $R = \{(r_o - r_i)/\ln(r_o/r_i)\}$ .

The measured strength of the tubes is as shown in Table 1. The maximum strength of 429 MPa was observed at the ambient temperatures. Macroscopic observation indicated that the samples shattered during testing and very often the fracture planes were at an angle (5–10°) from the tensile midplane. The strength of the oxide tube at 1000 °C in N<sub>2</sub> sharply decreased to a maximum of 226 MPa that is nearly half its value at the ambient condition (Table 1). The specimen had shattered during testing and fracture was observed to have deviated from the mid-plane.

For Weibull analysis, the failure probability was estimated from the expression

$$P_f = (n-0.5)/N_t, \quad (2)$$

where  $N_t$  is the total number of samples tested and  $n$  is the rank of a particular specimen. The resulting data were fitted to the two-parameter Weibull equation [30] to determine the Weibull modulus ( $m$ ) and characteristic stress ( $\sigma_0$ ). The observed variation in strength and the predominating flaw system for fracture was plotted on a Weibull graph as shown in Fig. 2. For specimens tested at 1000 °C in N<sub>2</sub>, although there was a reduction in

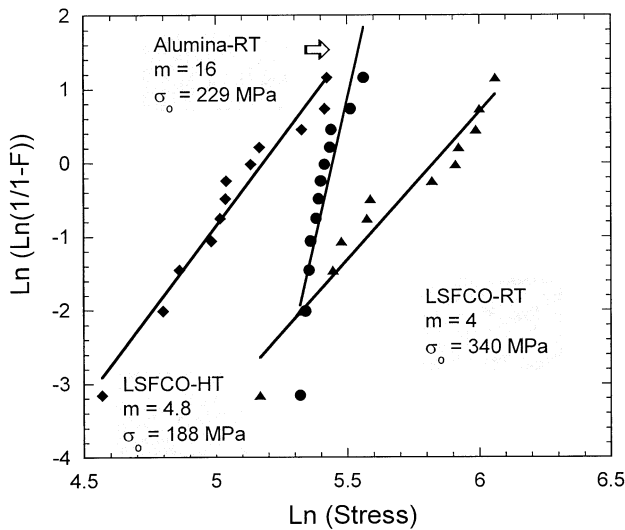


Fig. 2. Weibull plots of alumina and perovskite tubes at ambient and reducing conditions. In perovskite tubes, failure is predominantly from surface and volume flaws.

strength, a slight increase in Weibull modulus  $m$ , was also observed.

The C-ring tests for ceramic tubes, which demonstrate a lower strength, are more indicative of realistic properties of the tubes as they have a larger effective volume and surface area under stress and thus statistically increase the probability of finding a flaw of critical size. The 'as-received' LSFCO tubes expectedly show a much lower Weibull modulus ( $m = 4-5$ ), as compared to a surface finished Alumina ( $m = 16$ ). The lower value of ' $m$ ' in LSFCO tubes signifies the influence of specimen geometry and flaw distribution on the overall strength distribution. The observed variation in the Weibull parameters and strength values can thus be attributed to the following factors: (i) processing related flaw distribution viz. surface and volume flaws. Changes in the flaw distribution can occur due to various factors such as: additives added (distribution of volume pores arising from binder burn out), die used (surface flaws distribution) related to the processing of the tube; (ii) variation observed in the wall thickness and ovality of the tubes provided; (iii) orientation of the fracture plane with respect to the loading axis or to the axis of the tube. Variation in dimension of the C-ring can also significantly alter the stress distribution in the ring. Although fracture planes in the samples were not exactly at the midplane, the measured deviations were not too large to necessitate a detailed stress distribution. The equivalency from a computed stress profile for a C-ring test indicate that the fiber strains are nearly equivalent over a region described by  $\theta = 30^\circ$  and maximum stresses are not limited to the exact midplane of the specimen [24]; and (iv) inherent strength of the material. The first three factors affecting the strength distributions are invariably related to the processing route employed for processing

the tubes. However, the fourth factor can be correlated to the inherent strength of the material and should be seen as a function of the composition and characteristics of the base powder.

The strength of the perovskite membrane tube at  $1000^\circ\text{C}$  in  $\text{N}_2$  reduced to nearly half its value at the ambient condition. The decrease in strength is accompanied with a slight increase in the Weibull modulus as compared to at ambient conditions (4–4.8). Although this increase is not significant (the values may possibly converge with large number of tests), there is a possibility that the environmental conditions may have actually blunted the strength controlling surface flaws (dominating at room temperature) and the overall strength distribution then being controlled by the processing related volume flaws. As shown in Fig. 3c, the volume flaws distribution is augmented by the additional pores formed due to pull out of chromate phase precipitates at the grain boundaries.

### 3.2. Fracture analysis

All specimens tested in the present study exhibited brittle fracture. The macroscopic fracture morphology at ambient temperature was transgranular and predominantly jagged with interspersing planes of smooth fracture. Subsequent microscopic analysis (Fig. 3) indicated that surface and volume flaws controlled the fracture origins. The volume flaws were approximately of the order of  $5-10\ \mu\text{m}$  and occurred randomly in the microstructure. In samples tested at  $1000^\circ\text{C}$  in  $\text{N}_2$ , the fracture surface as also the outer surface of the tube appeared to have significantly roughened. The measured surface roughness increased to  $5.6\ \mu\text{m Ra}$  from an initial value of  $4.3\ \mu\text{m Ra}$  at room temperature. Microscopic analysis suggested that volume flaws (Fig. 3b) were dominating the fracture origins.

Fractured surfaces of samples tested at both ambient and reducing conditions showed that the material was composed of equiaxed grains. At room temperature, X-ray analysis indicated the dominant phase in the tubes to be the primitive cubic perovskite phase and fracture at an applied stress did not alter the structure. Samples fractured at  $1000^\circ\text{C}$  showed traces of decomposition products (Fig. 4). Microscopic analysis of fracture at ambient temperature indicated characteristic transgranular fracture with evidences of flat cleavage planes of brittle fracture and increased formation of pores at the grain boundaries (Fig. 5a). The additional pores formed could probably be due to pull out of precipitates of the chromate phase at triple point grain boundaries [31]. However, the exact contribution of the chromate phase at the grain boundary to the fracture strength of the material is still not clear. Micro-cleavage planes in the grains pointed towards activation of additional energy dissipative process during crack growth and thus



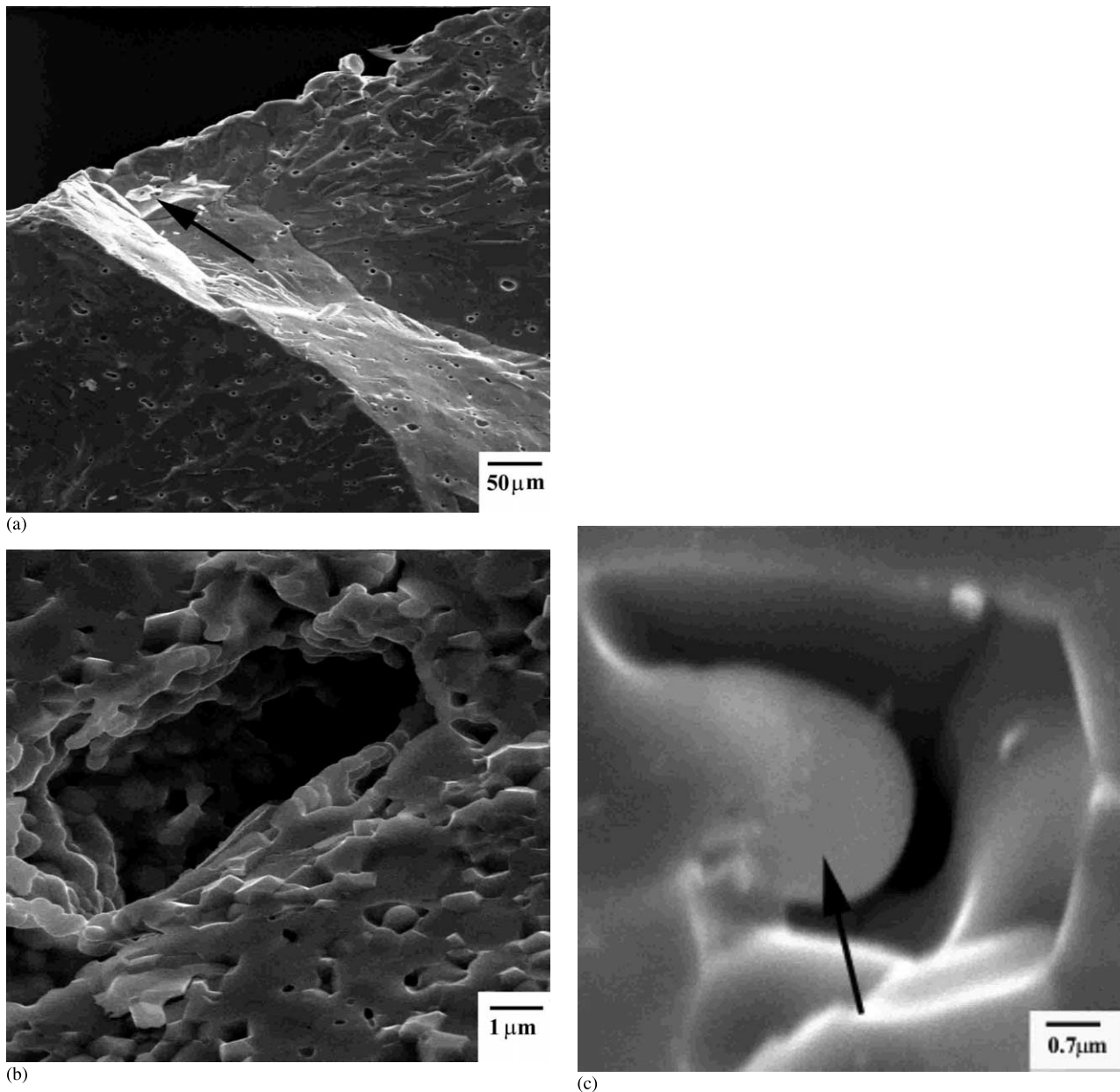


Fig. 3. SEM examination of the fracture surfaces indicating failure initiated by: (a) surface, (b) volume defects, and (c) additional pores formed at high temperatures due to phase formation.

promoting small scale toughening in the material. Samples tested at 1000 °C in N<sub>2</sub> showed a dramatic effect of the environment and temperature on the fracture morphology. The fracture surfaces showed increased density of pores probably due to the pullout of the (La,Sr)CrO<sub>3</sub> phase formed at grain-boundary triple points and grain-boundary cavitations (Fig. 3c). Moreover, the larger grains appeared to have broken down to finer particles and accentuated relief between the grains and the grain boundaries were observed (Fig. 5b). The grain boundary were approximately ~1–2 μm thick and the accentuated relief appeared to be similar to those observed in thermally etched surfaces of a

similar oxide [32]. The relief between the grain and the grain boundary seemed unlikely to be the effect of thermal etching since the test temperature was at least 500 °C lower than the sintering temperature and the residence time after fracture was only a few seconds before the test furnace was switched off. The accentuated grain boundary could be reasoned as due to the segregation of impurities or chemical inhomogeneity at the grain boundary. A higher magnified view of a single fractured grain shows clear evidence of precipitate formation and their pull out inside a grain (Fig. 6a and b). These precipitates were approximately 100 nm and appeared to have randomly formed between bands

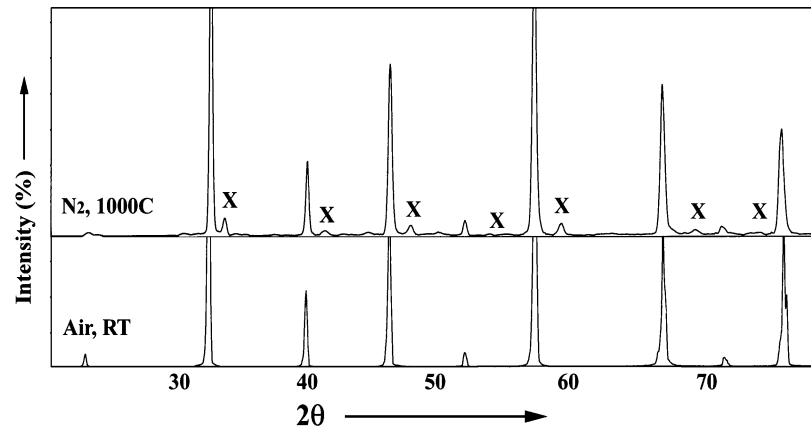


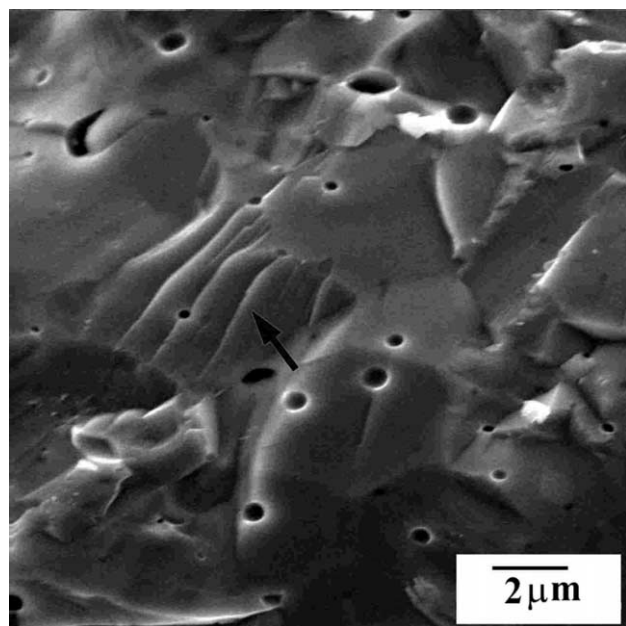
Fig. 4. X-ray analysis indicating formation of X-(La,Sr)CrO<sub>3</sub> while retaining the basic perovskite structure upon reduction in N<sub>2</sub> at 1000 °C.

of grain matrix (Fig. 6b). The bands inside the grain were approximately 150 nm with an average band spacing of 100 nm and indicated an orientation unique to the individual grain (Fig. 6a). The accentuated grain boundaries also exhibited bands but they were not in the same orientation as inside the grains.

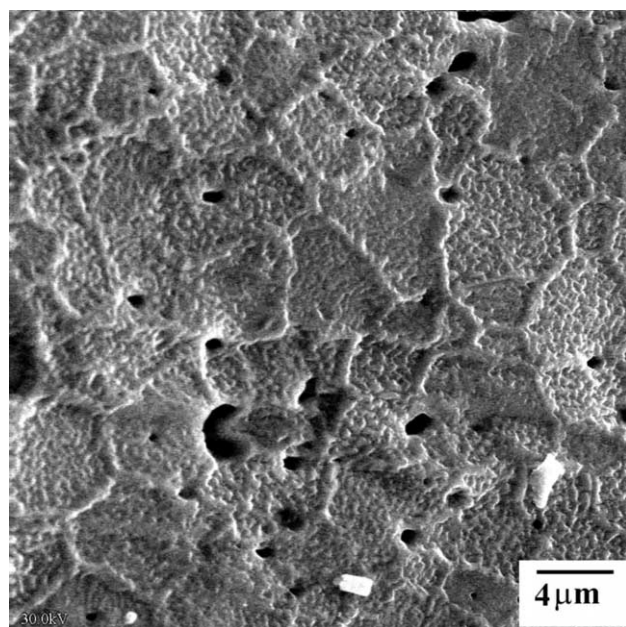
Energy dispersive X-ray (EDX) lines scan profiles across fractured grains indicated significant variation of the elements La, Sr, Fe and Cr. As a rule, the dominant peaks were from Sr and Fe; La concentration was coupled with Sr and Cr with Fe concentration, respectively. At ambient conditions, the grain boundaries tended to be richer in Strontium and leaner in Iron. In grains fractured at higher temperature (Fig. 6b), the dark bands were richer in Sr and Fe as compared to the brighter bands. Within each band, two distinct zones were noted: In the first zone, any increase in Sr, La and Cr concentration was accompanied with a decrease in Fe concentration. A zone in which with any increase in Fe and Cr was accompanied by a drop in La and Sr concentration alternated this. In contrast, the first zone in the bright band indicated an uniform rise in La, Sr, Fe and Cr concentration and was followed by a zone in which any rise in Fe concentration was accompanied by a drop in Cr, La and Sr concentration. The particles between the bands were observed to be richer in La, Sr and Fe as compared to the bands in the grains. The particles are probably the decomposed (La,Sr)Fe<sub>12</sub>O<sub>12</sub> phase. The grain boundaries were richer in Sr, while the grains tended to be Sr deficient. Within the grain boundary any increase in Sr was accompanied with an increase in La and a corresponding drop in both Fe and Cr. The increased Sr at the grain boundary corresponded well with previous observations concluding a build up of strontium at the grain boundaries with the strontium deficient grains acting as acceptors [33]. The enrichment of strontium probably via high diffusive paths at the grain boundaries could lead to the formation of point defects [34]. The formation of point defects could then enhance the diffusion of oxygen or metal

component via grain boundary and often govern the oxygen permeation, reaction and degradation of materials [35].

Phenomenologically, fracture in reducing conditions can be assumed to be controlled by oxygen diffusing relatively freely through the material at a rate that is controlled by temperature. The observed roughening of the specimen surface and microscopic fracture morphology could be thus attributed to the same. To gain further insight into the role of diffusing oxygen at the atomic scale, and its possible influence on fracture morphology, recourse was taken to the earlier work involving Z-contrast imaging and EEL spectra on the LSCFO membranes exposed to similar conditions [36]. This data was acquired from two different samples; one as sintered (untreated) and the second one previously heated to 1123 K and then exposed to reducing (N<sub>2</sub>) conditions (treated). During this cycle the material was reduced and a 2% expansion was measured. Fig. 5 shows the micrographs of the sintered and treated samples in the [001] orientation. The brighter spots represent the (La,Sr) columns, whereas the darker spots are the (Fe,Cr)–O columns. The treated sample shows a periodic change in contrast in every second (Fe, Cr)–O (indicated by arrows). The EEL spectra of the treated and untreated sample obtained with a broad electron beam at a low magnification (Fig. 7) show the oxygen K-edge and the chromium L<sub>3</sub>,L<sub>2</sub>-edges normalized to the continuum between the peaks. The most obvious changes in the spectra were the different oxygen K-edge fine structure and the lower intensity Cr L<sub>3</sub>-edge in the treated material. At comparable specimen thickness, the drastic reduction of the peaks at 532 eV and fewer counts under the oxygen K-edge confirm the overall oxygen reduction of the membrane and the column-by-column EEL spectra represent the oxygen, chromium, iron and lanthanum peak in the dark and bright columns. Comparison of different positions in the sample indicated that the intensity of the La L<sub>3</sub>,L<sub>2</sub>-peaks was constant all over the sample, so that normal-



(a)

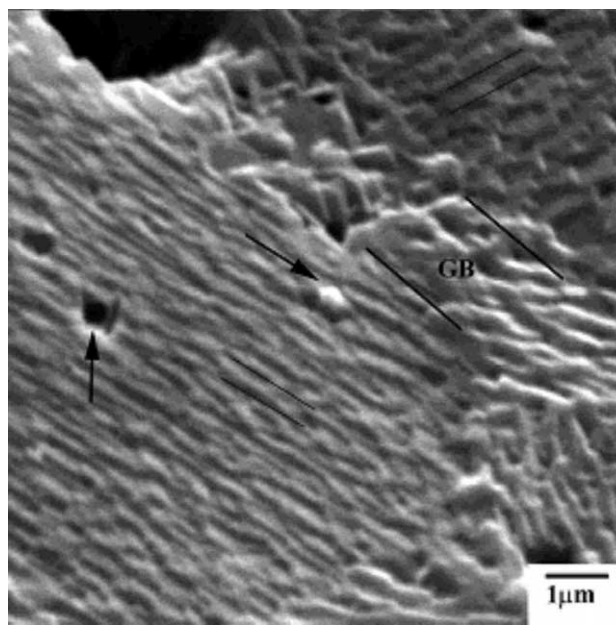


(b)

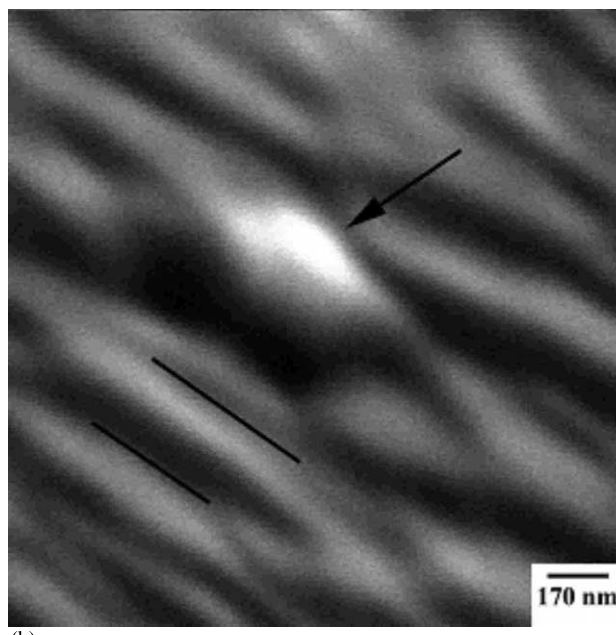
Fig. 5. Fracture observed in perovskite tubes in (a) at ambient conditions and (b) reducing conditions.

ization of the spectra to these peaks seemed reasonable. The spectra exhibited all the features that indicated lower oxygen content in the dark columns: reduction of the Fe- and Cr- $L_3$ , a change in the oxygen fine structure and a reduction of the pre-peak [37].

In-situ heating of the already treated sample gave further evidence of the kind of ordering in different columns. Apart from the broadening of the atomic columns, due to thermal vibration at 724 K the bulk (Fig. 8a) exhibited the same structural composition as at room temperature. The superstructure was still visible at



(a)



(b)

Fig. 6. Fracture in a single grain indicating: (a) band orientation in the grains, grain boundary with evidences of precipitate pull out and (b) dark and bright bands adjacent to a precipitate.

this temperature and atomic resolution EELS (Fig. 9b), normalized as described before, showed even larger differences. The pre-peak of the oxygen edge was further reduced and decrease of the B-site metal  $L_3/L_2$  ratio enhanced. The spectra calibrated in terms of formal valence acquired from iron oxides with varying iron valence under exactly the same conditions was used to calculate a fit function for all the possible iron valence states. With this method, it was possible to determine directly the formal valence of the B-site in the material and relate it to the number of oxygen vacancies. A compilation of the measured iron valences clearly



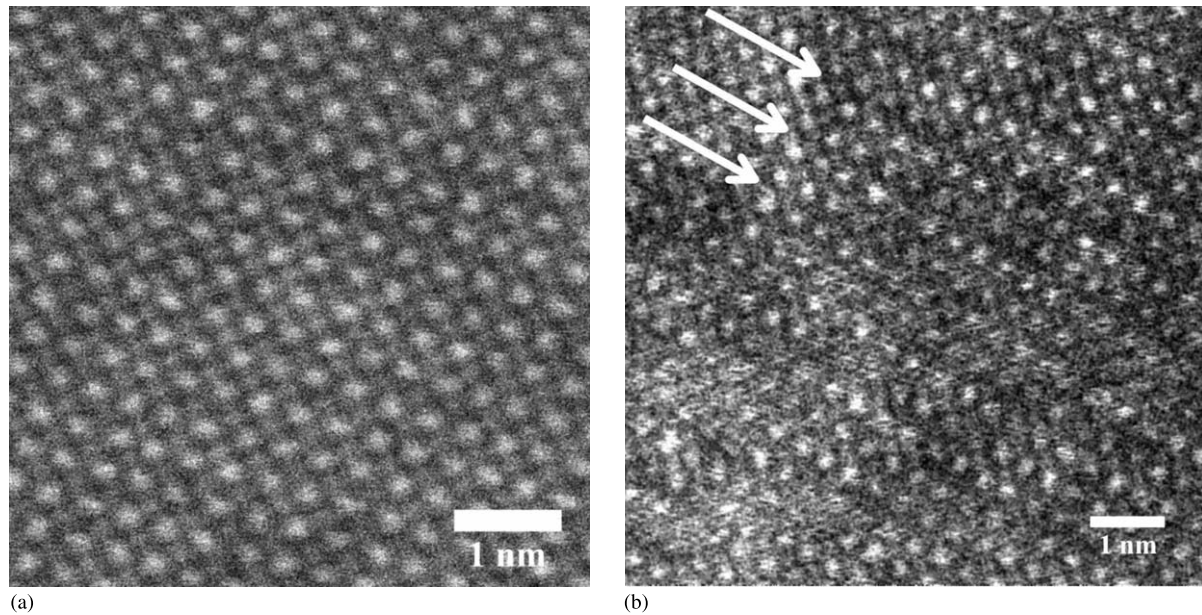


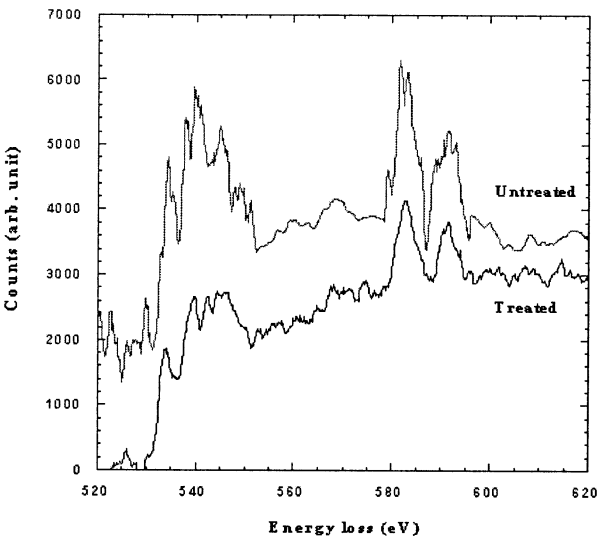
Fig. 7. Micrographs of LSCO in the [001] projection at (a) room temperature and (b) 724 K (arrows indicate the dark columns).

indicated that irrespective of the temperature, the iron valence in the bright columns remained constant at  $3+$ . However, a drastic difference in the number of oxygen atoms in the dark columns could be observed. At room temperature, the iron valence was  $2.3+(\delta=0.73)$  whereas at elevated temperature, the iron valence was reduced to  $2.1+(\delta=0.85)$ . This meant that the dark columns exhibited Brownmillerite like oxygen vacancy structures, where at elevated temperatures additional defects are produced. The Brownmillerite–Perovskite structural transitions could not be directly linked to distinctive morphological transitions observed in the fracture surfaces. However, it seems very likely that the transition bear considerable influence on the internal induced strain (lattice expansion caused by chemical reduction) and on the observed bands in the fractured grains.

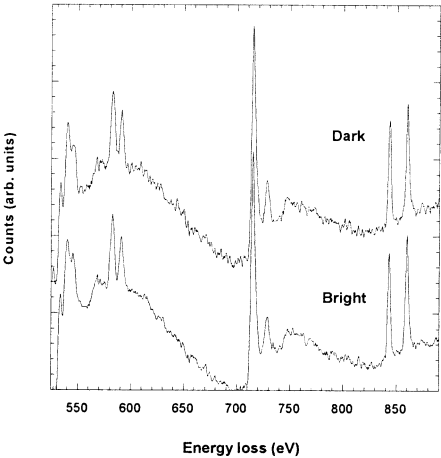
Assuming, that the total accumulated strain in the lattice can be written as the sum of the chemical strain and the elastic strain, at a first approximation, the chemical strain is expected to be proportional to the oxygen vacancy concentration and can therefore be characterized by a parameter,  $\epsilon_c/\delta$ . Where,  $\epsilon_c$  is the chemical strain measured with respect to a suitable reference state {e.g.  $\epsilon_c = (L - L_0)/L_0$  at oxygen activity of unity} and  $\delta$  the stoichiometry of the oxide. The parameter  $\epsilon_c/\delta$ , can be taken as an indicator of how much the lattice expands per oxygen vacancy and the chemical strain is observed to be proportional to the deviation in stoichiometry. The parameter is also observed to be influenced by structure and composition in the oxides (e.g.  $\epsilon_c/\delta$  increases with dopant concentration and decreases with increasing temperature) [38].

In LSCO tubular membranes, the measured expansion of the material ( $\approx 2\text{--}5\%$ ), in connection with the Brownmillerite ordering of the individual grains at low oxygen partial pressures [36] suggests to a induced strain at the internal interfaces. A measure of the induced strain can be calculated from the measured values of  $\delta$  in the material [39]. Assuming  $\epsilon_c$  to be in the order of  $0.0003\text{--}0.0025$  [40–42], the values of  $\epsilon_c/\delta$  for the two columns are as tabulated in Table 2. Significantly,  $\Delta\delta$  and  $\epsilon_c/\delta$  of the Brownmillerite structure (dark column) differ from that of the bright column by a factor of 10. The difference in the  $\epsilon_c/\delta$  parameter between the two columns is an indication of the stress at the interfaces between the two structures. The exact nature (tensile/compressive) of the internally induced stress is beyond the scope of this paper but can be assumed to result in an increased stress field at the grain boundaries. Moreover, structural changes in the lattice due to reduction of Fe and Cr could possibly reduce the cohesive strength of the lattice. The cohesive strength of the lattice is controlled by the fracture energy and elastic modulus of the material [43] both of which can undergo changes with annealing at low oxygen pressures resulting in lowered grain strength. The increased stress level and lowered grain strength manifest in increased propensity for transgranular fracture and accentuate the relief between the grain and grain boundaries as observed at high temperature (Fig. 5b). However, it is to be noted that the random orientation of the grains in these polycrystalline materials prohibits a homogeneous expansion in all three dimensions, which would act to decrease the overall stress and strain in the membrane. A more detailed characterization is thus required to identify whether the ordering of the oxygen vacancies





a)



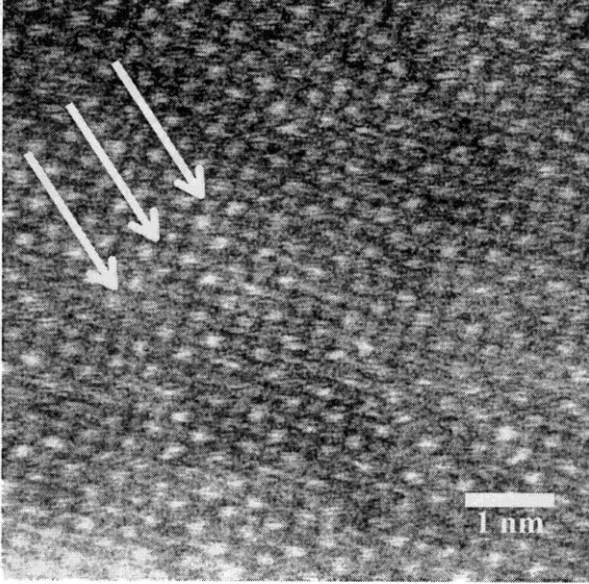
b)

Fig. 8. (a) EEL spectra at low magnification from the untreated and treated sample. (b) Column-by-columns EELS in the treated sample from the bright and dark columns at room temperature.

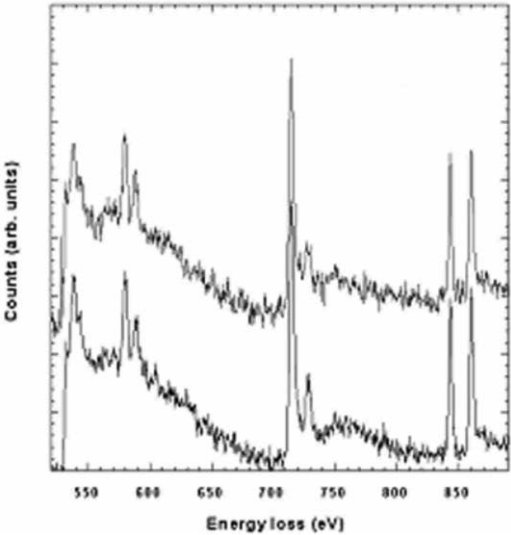
leading to phase transitions in LSFCO perovskites does provide the necessary driving force for controlling the preferred fracture paths.

4. Conclusions

(1) LSFCO perovskite have been investigated to provide directly pertinent information on strength and fracture mechanism when processed as tubular membranes for application in separation reactors. The strength of the single-phase perovskite tube in slightly reducing conditions decreases to nearly half its value at ambient conditions (186 and 307 MPa, respectively). Fracture at both the conditions is primarily controlled



(a)



(b)

Fig. 9. (a) Micrograph in the [001] projection of the treated LSFCO at 724 K, (b) EEL spectra from the dark and bright columns at 724 K (arrows indicate the dark columns).

Table 2  
Comparison of valence structures and calculated chemical strain in LFSCO grains at 723 K

Structure	$\delta_{\text{air}}$	$\delta_{\text{HT}}$	$\Delta\delta$	$\epsilon_c/\delta$
Perovskite (bright column)	$0.43 \pm 0.05$	$0.44 \pm 0.05$	$0.01 \pm 0.05$	$0.03-0.25$
Brownmillerite (dark column)	$0.74 \pm 0.05$	$0.84 \pm 0.05$	$0.10 \pm 0.05$	$0.003-0.025$

by processing related defects such as surface flaws, pores, etc. However, the flaw population does not significantly alter the high temperature strength distribution (Weibull parameter ' $m$ ') in the oxide tubes.

(2) Fracture in the tubular membranes is by transgranular cleavage of the equiaxed grains. Micro cleavage planes observed in individual grains points indicates activation of small scale toughening process. Also evidences of precipitate (chromate phase) pull out at triple point grain boundaries are seen. Samples tested in reduced conditions, indicate roughening of the surface. Subsequent microscopic analysis reveal accentuated relief between the grains and the grain boundaries probably due to segregation of elements and internal stresses. In addition, secondary phases at the phase junctions are formed during the heating and reduction process. The secondary phases formed are probably the decomposition product  $(\text{La,Sr})\text{CrO}_3$ . The precipitates inside the grains could probably be the decomposed  $(\text{La,Sr})\text{Fe}_{12}\text{O}_{12}$  phase.

(3) EEL spectra confirm the overall reduction in the membrane material. The active diffusion mechanisms in LSCFO are observed to be controlled by the oxygen vacancies in the bulk. The oxygen vacancies are created by the acceptor A-site doping and are accompanied by the reduction of Fe and Cr at the B-site.

(4) The ordering of the oxygen vacancies into the Brown-millerite phase leads to lattice expansion in one dimension. This will introduce additional stress at the grain boundaries.

(5) The interactions between the dopant ions, oxygen vacancies, structure and/or phase transitions significantly influence the strain in the lattice. The interaction influences the fracture morphology and probably manifests in the formation of bands in the fractured grains.

(6) The preferred fracture paths in the LSCFO membrane are possibly controlled by phase transition aided by reducing conditions and applied stress. The concentration of the oxygen vacancies in the membranes could significantly alter the stress distribution in the tubular membrane.

## Acknowledgements

This research was sponsored by National Energy Technology Laboratory, US Department of Energy under grant number DE-FC26-99FT40054. We thank Drs T.J. Mazanec and W.T. Stephens for providing the samples for the present study.

## References

- [1] S. Ling, Phys. Rev. B 49 (2) (1994) 864–880.
- [2] Y.M. Chiang, D. Birnie, W.D. Kingery, Physical Ceramics, MIT Series (1997).
- [3] M.H.R. Lankherst, H.J.M. Boumeester, H. Verweij, J. Am. Ceram. Soc. 58 (1985).
- [4] S.C. Singhal, MRS Bull. 3 (2000) 16.
- [5] T. Ekstrom, R.J.D. Tilley, Chem. Scripta 16 (1980) 1.
- [6] K. Huang, R.S. Tichy, J.B. Goodenough, J. Am. Ceram. Soc. 81 (1998) 2565–2575.
- [7] T.J. Mazanec, Solid State Ionics 70/71 (1994) 11–19.
- [8] H. Kruidhof, H.J.M. Boumeester, R.H.E. v. Doorn, A.J. Burggraaf, Solid State Ionics 63-65 (1993) 816–822.
- [9] Z.L. Wang, Z.C. Kang, Functional and Smart Materials, Plenum Press, New York, 1998.
- [10] C.N.R. Rao, J. Gopalakrishnan, K. Vidyasagar, Indian J. Chem. 23A (1984) 265.
- [11] Z.L. Wang, J. Zhang, Phys. Rev. 54 (2) (1996) 1153–1158.
- [12] S. Stemmer, A. Sane, N.D. Browning, T.J. Mazanec, Solid State Ionics 130 (1-2) (2000) 71.
- [13] R.F. Klie, Y. Ito, S. Stemmer, N.D. Browning, Ultramicroscopy, 86 (2001).
- [14] N.M. Sammes, R. Ratnaraj, M.G. Fee, J. Mater. Sci. 29 (1994) 4319.
- [15] N.M. Sammes, R. Ratnaraj, J. Mater. Sci. 30 (1995) 4523.
- [16] N.M. Sammes, F.M. Keppeler, H. Näfe, F. Aldinger, J. Am. Ceram. Soc. 81 (1998) 3104–3108.
- [17] S.W. Paulik, S. Baskaran, T.R. Armstrong, J. Mater. Sci. 33 (1998) 2397.
- [18] J.W. Stevenson, T.R. Armstrong, L.R. Pederson, J. Li, C.A. Lewinsohn, S. Baskaran, Solid State Ionics 113–115 (1998) 571.
- [19] S. Baskaran, C.A. Lewinsohn, Y.S. Chou, M. Qian, J.W. Stevenson, T.R. Armstrong, J. Mater. Sci. 34 (1999) 3913.
- [20] S.W. Paulik, S. Baskaran, T.R. Armstrong, J. Mater. Sci. Lett. 18 (1999) 819.
- [21] C.M. D'Souza, N.M. Sammes, J. Am. Ceram. Soc. 83 (2000) 47–52.
- [22] M.P. Pechini, U.S. Pat. No. 3,330,697, 1967.
- [23] N.G. Eror, H.U. Anderson, Better Ceramics through Chemistry II, In: C.J. Brinker, D.E. Clark, D.R. Ulrich (Eds.), Proceedings of Materials Research Society Symposium, Palo Alto, CA, April 1986. Materials Research Society, Pittsburgh, PA, 1986, pp. 571–771.
- [24] M.K. Ferber, V.J. Tennery, S. Walters, J.C. Ogle, J. Mater. Sci. 8 (1986) 2628.
- [25] ASTM C 1323-96, American Society for Testing and Materials, (1996) 547.
- [26] P.D. Nellist, S.J. Pennycook, Ultramicroscopy 78 (1999) 111.
- [27] R.T. Egerton, Electron Energy Loss Spectroscopy in an Electron Microscope, Plenum, New York, 1996.
- [28] E.M. James, N.D. Browning, Ultramicroscopy 78 (1999) 125.
- [29] G.R. Anstis, P. Chantikul, B.R. Lawn, D.B. Marshall, J. Am. Ceram. Soc. 64 (9) (1981) 533–538.
- [30] W. Weibull, J. Appl. Mech. 18 (1951) 293.
- [31] Private Communications.
- [32] C. Tsai, A.G. Dixon, Y.H. Ma, W.R. Moser, M.R. Pascucci, J. Am. Ceram. Soc. 81 (1998) 1437–1444.
- [33] A.C. Palunduz, Private Communications.
- [34] Private Communications.
- [35] N. Sakai, T. Horita, H. Yokokawa, M. Dokiya, T. Kawada, Solid State Ionics 80–88 (1996) 1273–1278.
- [36] R.F. Klie, N.D. Browning, J. Electron. Microsc. (2002) 559–566.
- [37] C. Collier, T. Mamorabi, C. Ortis, Phys. Rev. B 44 (1991) 1201.
- [38] A.I. Yasuda, M. Hsinihuma, Electrochem. Soc. Proc. (1997) 97–124.
- [39] A. Atkinson, T.M.G.M. Ramos, Solid State Ionics 129 (2000) 259–269.
- [40] T.R. Armstrong, J.W. Stevenson, L.R. Pederson, P.E. Raney, J. Electrochem. Soc. 143 (1996) 2919–2925.

- [41] P.H. Larsen, P.V. Hendriksen, M. Morgensen, J. Thermal Anal. 29 (1997) 1263–1275.
- [42] K. Mori, H. Miyamoto, K. Takenobu, T. Matsudaira, In: U. Stimming, C. Singhal, H. Tagawa, W. Lehnert (Eds.), Proceedings of the Fifth International Symposium on Solid Oxide Fuel Cells, Vol. 97–40, The Electrochemical Society, 1997, pp. 1301–1305.
- [43] S.M. Weiderhorn, In: J.B. Wachtman Jr. (Ed.), Mechanical and Thermal Properties of Ceramics, National Bureau of Standards (US) Special Publication 303, National Bureau of Standards, Washington, DC, 1969, p. 217.